metals

MDPI

Article

Effects of Oxidation on the Cracking Behavior of Additive-Manufactured Cobalt-Based Alloys Under Thermal Fatigue Conditions

Xudong Yang [1,2,3,*], Zixian Jiao [1,2,3], Jiayue Xu [1,4], Xinyu Zhang [5] and Yi Xie [1,2]

[1] Shanghai Institute of Space Propulsion, Shanghai 201114, China; jiaozixiansisp@163.com (Z.J.); xujiayue@mail.nwpu.edu.cn (J.X.); xieyisisp@163.com (Y.X.)
[2] State Key Laboratory of Advanced Space Propulsion, Shanghai 201114, China
[3] Xinchang Tianqi Institute of Astronautics and Aeronautics, Shaoxing 312500, China
[4] National Elite Institute of Engineering, Northwestern Polytechnical University, Xi'an 710072, China
[5] State Key Laboratory of Advanced Special Steel, School of Materials Science and Engineering, Shanghai University, Shanghai 200444, China; zhangxinyu996@shu.edu.cn
* Correspondence: xdyang801@126.com

Abstract

Stellite alloys are widely used in the aerospace field owing to their excellent high-temperature strength and thermal fatigue resistance. However, with the rapid development of the aerospace industry, there is an urgent demand to further enhance the mechanical properties and thermal fatigue resistance of Stellite alloys. In the present study, we prepared a conventional CoCrW alloy (classified as a Stellite alloy) and a novel CoCrWAlNi alloy, which was formulated by introducing aluminum and nickel into the CoCrW matrix, using the direct laser deposition technique. Their microstructural characteristics, mechanical properties, and thermal fatigue performance were systematically investigated. The results indicated that the additions of aluminum and nickel contribute to stabilizing the γ-Co phase. Compared with the CoCrW alloy, the CoCrWAlNi alloy exhibited higher elongation at fracture. In situ observation was employed to study the initiation and propagation of thermal fatigue cracks. Meanwhile, the effects of oxidation on thermal fatigue resistance were analyzed through experimental tests and theoretical calculations based on the Huntz model. Finally, an optimized thermal fatigue mechanism tailored for cobalt-based alloys was established, which yields deeper insights into the failure mechanisms of these alloys under complex thermal-cycling fatigue conditions.

Keywords: thermal fatigue; CoCrWAlNi alloy; direct laser deposition; oxidation

Check for updates

Academic Editor: Rebecca L. Higginson

Received: 20 February 2026
Revised: 22 March 2026
Accepted: 24 March 2026
Published: 31 March 2026

Copyright: © 2026 by the authors. Licensee MDPI, Basel, Switzerland. This article is an open access article distributed under the terms and conditions of the Creative Commons Attribution (CC BY) license.

1. Introduction

As a critical component of rocket engines, the regenerative cooling nozzle participates in key processes including the generation of high-temperature combustion gas and its expansion, acceleration, and ejection [1]. By flowing through the internal cooling channels of the nozzle before entering the injector, the fuel or oxidizer effectively reduces the inner wall temperature, improves energy utilization efficiency, and prolongs the service life of the nozzle. However, such severe thermal cycling tends to induce thermal fatigue (TF) failure, as the temperature rapidly rises to several hundred degrees Celsius within seconds and then drops just as quickly [2]. TF is one of the primary factors responsible for performance degradation and service life reduction in rocket engines for aerospace applications [3]. Furthermore, as space endeavors (e.g., deep space exploration) continue to evolve, more

stringent performance criteria have been placed on rocket engines, such as enhanced specific impulse and increased thrust output; these demands, in turn, entail a far more extreme operating environment. Cobalt-based alloys are extensively employed as rocket engine nozzles, owing to their exceptional mechanical strength and toughness [4–6]. Extensive research has been conducted on the microstructural characteristics, phase transformation behaviors, and mechanical properties of CoCrW alloys, while recent studies have focused on strategies to enhance their TF resistance [4]. Specifically, the TF resistance of cobalt-based alloys can be enhanced via alloying approaches. For instance, the addition of manganese stabilizes the ε-Co phase during the TF process, thereby reducing crack propagation rates [7]. In addition, Wu et al. [8] demonstrated that the additions of titanium and nickel (Ni) to CoCrW alloys effectively suppress TF crack propagation by reducing carbide precipitation and improving material toughness. Furthermore, the CoNiTi alloy has been developed, which presents excellent TF resistance compared with CoCrMoW and Stellite 6 alloys [9].

A defining feature of TF is the rapid cycling of temperatures, which generates substantial thermal stress throughout the process [10]. When alloys undergo TF process, volume variation, thermal expansion coefficient mismatch, and temperature gradients are the core drivers of damage initiation and evolution [11]. Wen et al. [12] investigated the microstructural evolution of cobalt-based alloys during thermal fatigue and found that new precipitates appeared around the carbides under thermal fatigue cycling conditions, thereby causing stress concentration. Oxidation also plays a critical role in TF, contributing synergistically to the processes of crack nucleation and propagation [13–15]. The formation and spalling of oxide films exert a significant impact on TF resistance, whereas the growth rate and interfacial adhesion of the oxide layer determine its protective efficacy [16]. Cracks form on the sample surface during thermal shock, and their propagation is driven by multiple stresses, including those induced by volume variation, mismatch in coefficients of thermal expansion (CTEs), and temperature gradients between the matrix and internal oxides [17].

Therefore, creep deformation, cyclic fatigue damage, oxidation reactions, and oxidation-induced stress must all be considered as synergistic factors during TF analysis [18,19]. Wagner was the first to investigate transient oxidation, and he deduced the formation conditions of the most thermodynamically stable oxide in binary alloys where both constituent elements are oxidizable [20]. Subsequently, Gesmundo et al. [21–24] explored the complex oxidation behaviors of binary two-phase alloys and proposed a semi-quantitative criterion for the formation of protective oxide layers. However, the oxidation process is governed by multiple factors, including the composition, spatial distribution, volume fraction, and microstructural characteristics of the two phases [25]. Considering these influences, the potential modes of high-temperature oxidation under low oxidant partial pressures have been examined, revealing that oxygen diffusion kinetics and the interdiffusion coefficients of the two alloying elements exert a dominant effect [26]. Notably, internal oxidation—an important oxidation process in binary two-phase alloys—is far more complex than that in single-phase alloys, as it involves the selective conversion of specific alloy components into oxides [27]. It has been reported that a critical chromium (Cr) concentration of 15–25 wt.% is required to form a continuous and stable chromium oxide layer during the oxidation of Co-Cr alloys [28,29]. Nevertheless, the presence of other alloying elements and the precipitation status of secondary phases can alter this critical Cr concentration and modify the morphology of the formed oxides [30]. Furthermore, oxidation during TF is synergistically affected by thermal stress and creep deformation, making it far more complex than oxidation under static, isothermal conditions; to date, no precise mechanism has been established to describe this process [31].

In the present study, CoCrWAlNi and CoCrW alloys were fabricated via direct laser deposition (DLD)—a representative additive manufacturing technology. The primary objective was to add aluminum (Al) and Ni in cobalt-based alloys to inhibit the rapid oxidation of carbides and thereby improve TF resistance. The TF process was systematically characterized, and microstructural changes before and after TF testing were analyzed in detail. In addition, the coupled creep-diffusion-oxidation stress field was quantitatively calculated, and a corresponding TF model was established. This work elucidates the mechanism by which Al and Ni additions modulate TF resistance, providing a theoretical basis for the compositional optimization of cobalt-based alloys.

2. Materials and Methods

2.1. Materials and DLD Process

The powders were prepared by adding 2 wt.% Al and 25 wt.% Ni into CoCrW commercial powders and mixing in a planetary ball mill (QM-2SP12, NanDa Instrument, Nanjing, China) for 5 h at 100 rpm. Table 1 lists the chemical compositions of the powders used to fabricate the alloys by DLD. Figure 1a shows that the DLD equipment comprises a 1070 nm-wavelength ytterbium fiber laser system (YLS-2000, IPG, Marlborough, MA, USA) and a robot (Rx160, Staubli, Pfäffikon, Switzerland) to mechanically operate the movement. The substrate was AISI H13 steel and a two-layer deposition was manufactured by DLD under argon for protection. A zigzag scanning strategy was adopted, where the deposition speed of the first (bottom) layer was 6 mm/s and that for the second (top) layer was 4 mm/s. The laser power, powder flow rate, and gas flow were set as 800 W, 8 g/min, and 12 L/min, respectively.

Table 1. Chemical composites of CoCrW and CoCrWAlNi powders (wt.%).

Alloy	Cr	W	C	Si	Fe	Al	Ni	Co
CoCrW	31.74	4.48	0.88	1.18	1.41	/	/	Bal.
CoCrWAlNi	23.17	3.27	0.64	0.86	1.03	2	25	Bal.

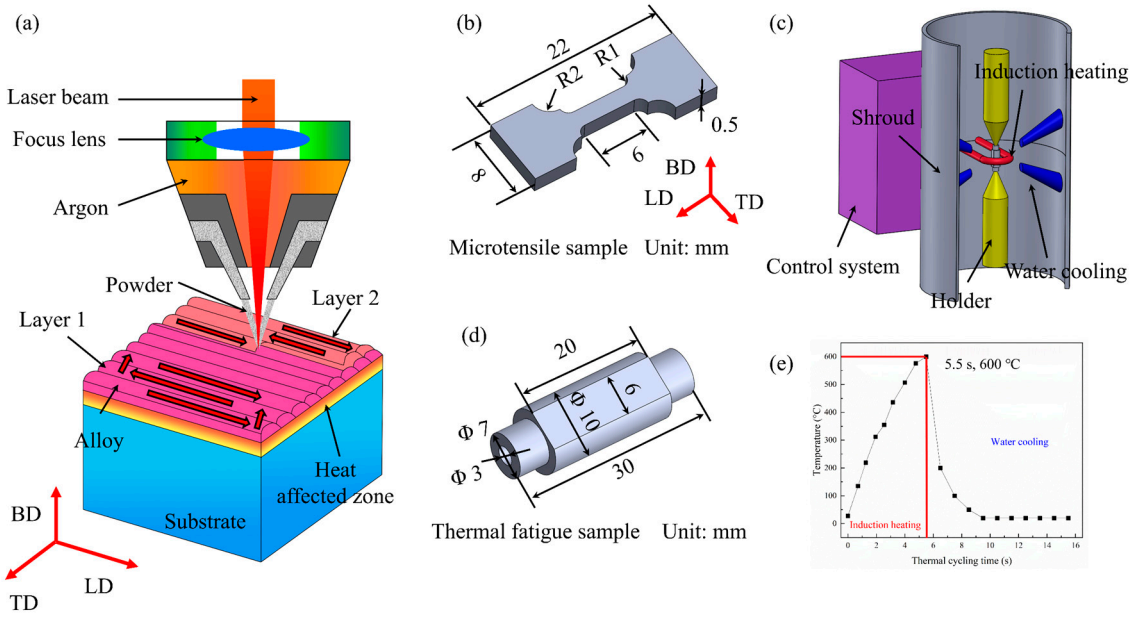


Figure 1. Schematic diagram of the DLD process, specimens, and TF test. (**a**) DLD technology, (**b**) tensile sample geometry, (**c**) TF equipment, (**d**) TF sample, and (**e**) heating and cooling cycle.

2.2. Microtensile Testing and Thermal Fatigue Testing

Microtensile tests were conducted at room temperature, and the samples were machined to the geometry shown in Figure 1b, which was designed according to International Standard ISO-6892-1 [32]. The specimen thickness was set to 0.5 mm, since TF cracks predominantly initiate from the surface. Thus, surface-layer metals were carefully extracted to enable a reliable comparison of mechanical properties. All the samples were ground and polished to ensure the same surface roughness. Microtensile tests were conducted on a 5 kN screw machine (MTEST5000W Tensile Stage, GATAN, Abingdon, UK) at a displacement rate of 0.1 mm/min under an in situ scanning electron microscope (SEM, LYRA3GMU, TESCAN, Brno, Czech Republic). The deformation was measured by the movement of the speckle pattern on the gauge section, which was deposited before the test. Three specimens were prepared for each alloy and subjected to microtensile testing, and the tensile data presented are the average values obtained from three independent measurements.

The TF test parameters were set with reference to the operating conditions of a certain type of engine: the temperature was raised to 600 °C within 5.5 s and then cooled down to room temperature within 10 s. The TF test was performed using the testing apparatus, and the dimensions are shown in Figure 1d. The test involved cyclic heating and water cooling, and a schematic diagram is shown in Figure 1c; the TF cycle is illustrated in Figure 1e. The temperature was measured using a K-type thermocouple. Three replicate specimens were also prepared for each material for thermal fatigue testing.

2.3. Microstructure Characterization

The microstructural morphologies of the samples before and after the tensile and TF tests were observed by scanning electron microscope (SEM) equipped with an energy dispersive spectroscope (EDS; Aztec X-MaxN, Oxford, UK) and electron backscatter diffraction (EBSD; HKL Nordlys Max3, Oxford, UK). The phase constituents and surface oxides of the alloys were characterized by X-ray diffraction (XRD; Ultima IV, Rigaku, Tokyo, Japan) and X-ray photoelectron spectroscopy (XPS; AXIS Ultra DLD, Tokyo, Japan), respectively. The TF process was observed using SEM and a laser scanning microscope (LSM, 900, Zeiss, Oberkochen, Germany).

3. Results

3.1. Microstructures and Tensile Properties of DLD Manufactured Alloys

As shown in Figure 2a,b, both alloys consist of fine dendrites and network-shaped eutectic structures. Under backscattered electron (BSE) imaging, the contrast in image intensity corresponds to chemical composition differences between the matrix and precipitated phases. The area fraction of precipitates in the CoCrW alloy is 20%, which is higher than the 14% measured in the CoCrWAlNi alloy. The overall cross-sectional morphologies of the two alloys are shown in Figure 2c,d, with a thickness of approximately 1 mm. The tensile specimens were machined from the surface to a depth of 0.5 mm in the middle region. As listed in Table 2, the compositions of the cladded alloys are close to that of the original powder according to the EDS analysis.

Table 2. Chemical composites of the points in Figure 2c,d (wt.%).

Location	Cr	W	C	Si	Fe	Al	Ni	Co
Sp1	30.59	4.05	1.02	2.14	1.05	/	/	61.15
Sp2	25.18	4.01	0.96	1.21	0.95	1.82	25.81	40.06

XRD analysis (Figure 2e) reveals that both alloys contain γ-Co, $M_{23}C_6$, and M_7C_3 phases, whereas ε-Co is only detected in the CoCrW alloy. The γ-Co matrix is formed during solidification, and eutectic carbides precipitate within the interdendritic regions, mainly consisting of $M_{23}C_6$ and M_7C_3. Owing to the low stacking fault energy (SFE) of the CoCrW alloy [33], ε-Co is generated from γ-Co via strain-induced martensitic transformation during cooling. The additions of Al and Ni elements increase the stacking fault energy of the alloy, which favors the nucleation and propagation of twins and dislocations rather than martensitic phase transformation [8].

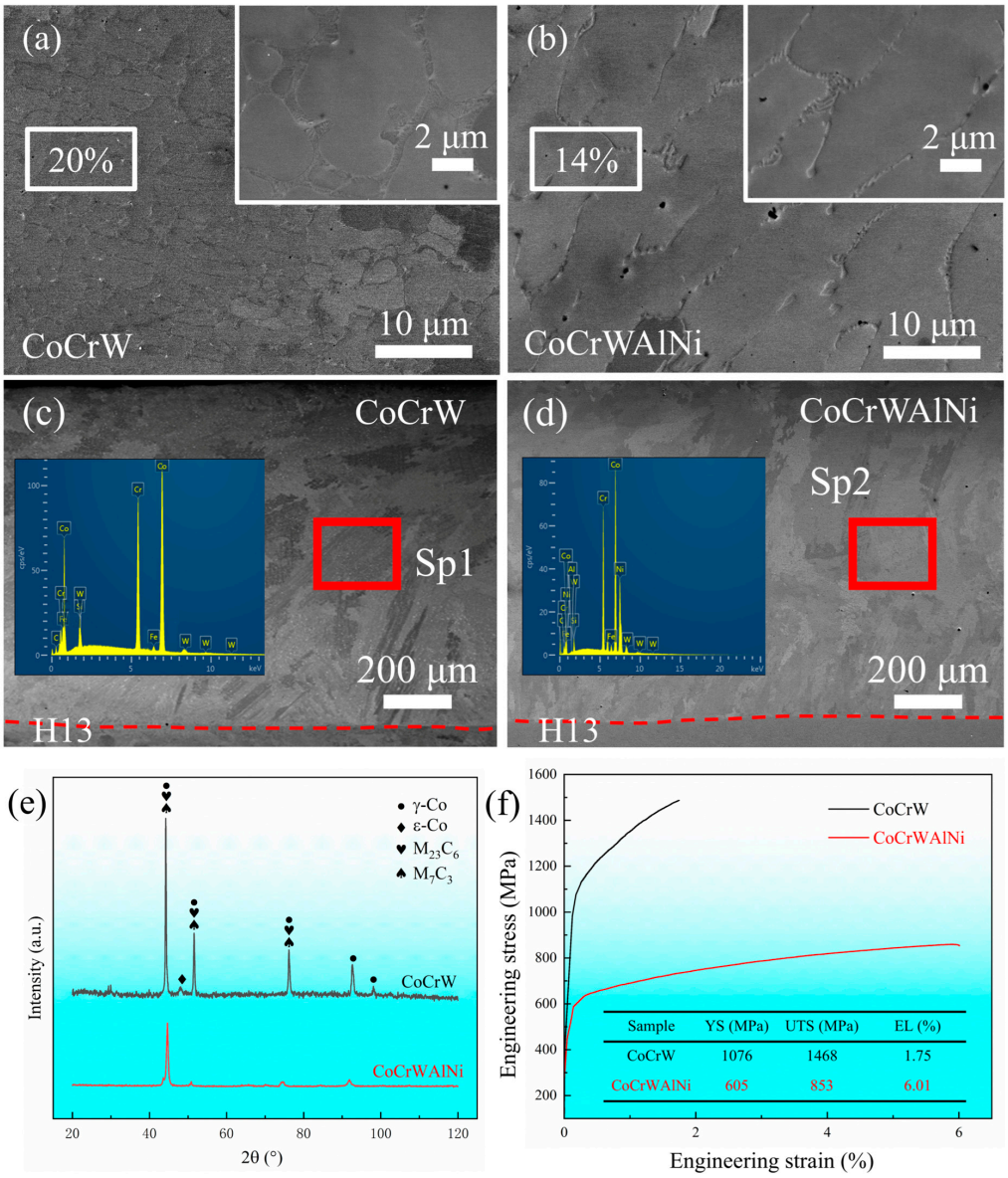


Figure 2. SEM micrographs of (**a**) CoCrW and (**b**) CoCrWAlNi; cross-sectional view of (**c**) CoCrW and (**d**) CoCrWAlNi; (**e**) XRD patterns, (**f**) Engineering stress–strain curves.

Figure 2f displays the engineering stress–strain curves of the CoCrW and CoCrWAlNi alloys. Although the CoCrW alloy exhibited higher ultimate tensile strength and yield strength than the CoCrWAlNi alloy, its plasticity was considerably poor. The additions of Al and Ni elements improved the ductility effectively, and the CoCrWAlNi alloy achieved an elongation of 6%.

Figure 3a,b present the fracture morphologies of the two alloys, which were analyzed to characterize their deformation and fracture behaviors. Although the two metals exhibit

similar microscopic fracture characteristics with dimples observed in both, it can be seen from Figure 3c,d that the fracture surface of the CoCrW alloy is relatively flat with low elongation. In contrast, the CoCrWAlNi alloy shows a more tortuous fracture surface, indicating improved ductility.

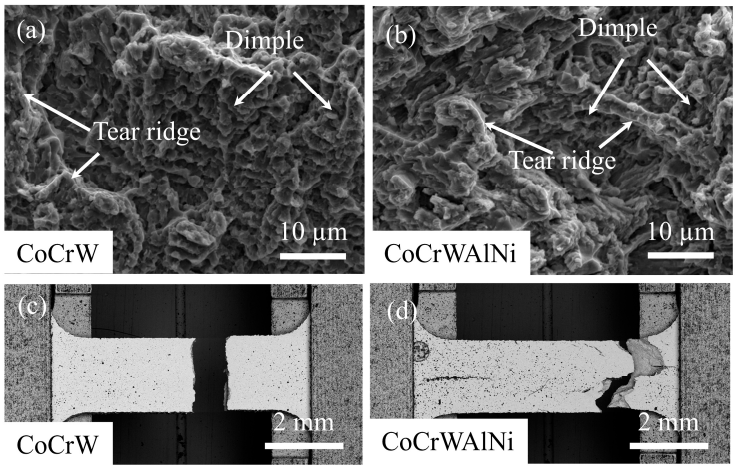


Figure 3. SEM images of fractures of (**a**) CoCrW and (**b**) CoCrWAlNi; SEM image of microtensile after breaking of (**c**) CoCrW and (**d**) CoCrWAlNi.

3.2. Thermal Fatigue Performance of DLD Manufactured Alloys

Figure 4 presents the initiation and propagation of cracks in the CoCrW and CoCrWAlNi alloys. The surface morphologies were observed by SEM and LSM at intervals of every 100 TF cycles. The critical TF cycles were defined as the number of cycles required for the crack length to exceed 50 μm at the central region of the samples. The average crack growth rate was determined as the ratio of the change in surface crack length to the corresponding number of cycles. Compared with the CoCrW alloy, the CoCrWAlNi alloy exhibited an increase in critical TF cycles from 1700 to 2200. Meanwhile, the average crack growth rate decreased from 0.023 μm/cycle to 0.015 μm/cycle along the length direction and from 0.04 μm/cycle to 0.035 μm/cycle along the depth direction. In order to reveal the TF mechanism and the differences in TF resistance between the two alloys, in situ TF tests were carried out.

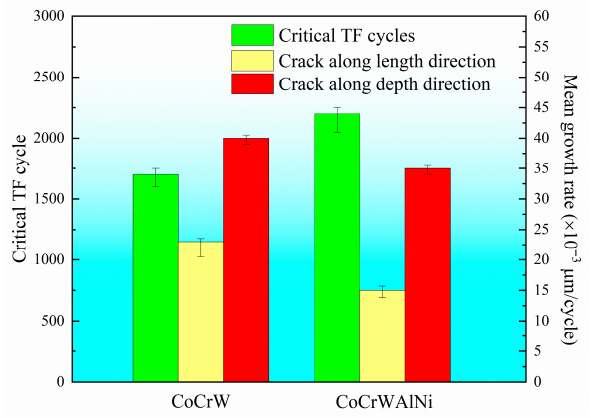


Figure 4. TF cracks initiation and propagation for the CoCrW and CoCrWAlNi alloy.

Figures 5 and 6 respectively illustrate the crack evolution of the CoCrW and CoCrWAlNi alloys from their critical TF cycles up to 3000 cycles. All samples were subjected to 3000 TF cycles to monitor the initiation and propagation of cracks. It can be observed that TF cracks propagate rapidly once initiated. The TF cracks initiated earlier and grew faster

in the CoCrW alloy than in the CoCrWAlNi alloy. Moreover, surface oxidation was found to develop preferentially along the cracks, indicating that TF behavior is associated with oxidation, in addition to the abrupt temperature variation.

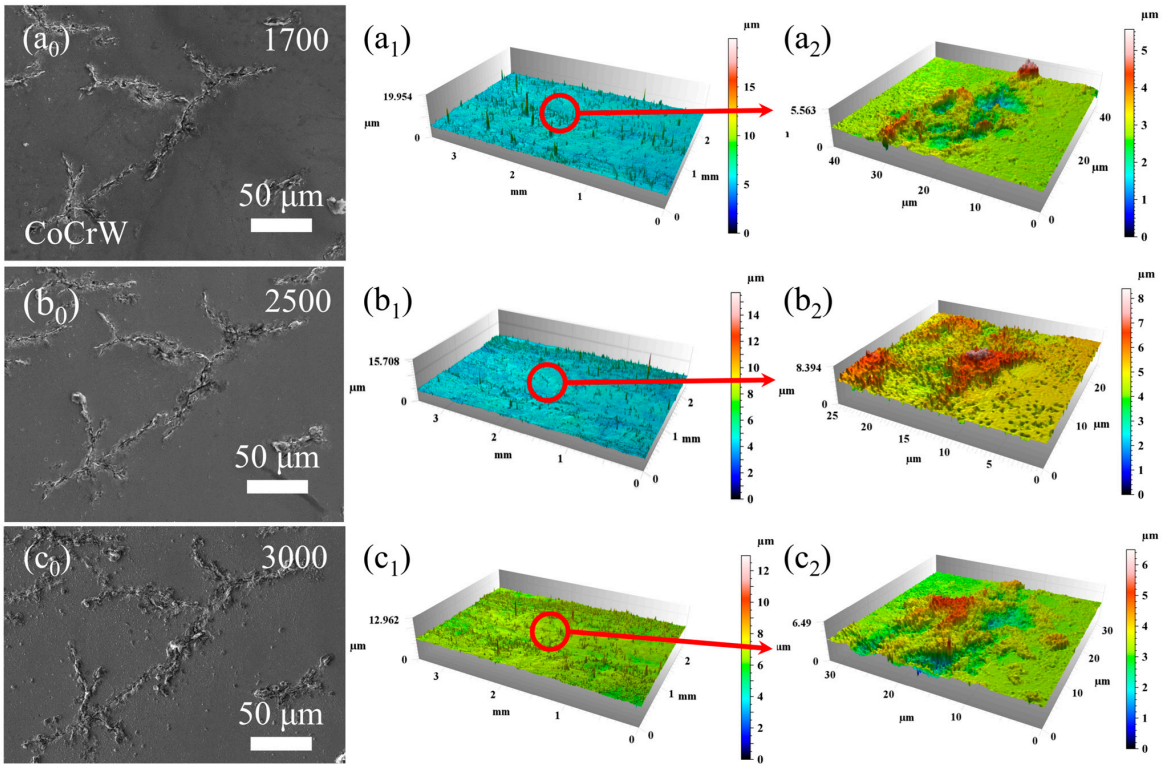


Figure 5. SEM and LSM images of TF racks of CoCrW at different cycles of (**a$_0$**–**a$_2$**) 1700, (**b$_0$**–**b$_2$**) 2500, (**c$_0$**–**c$_2$**) 3000.

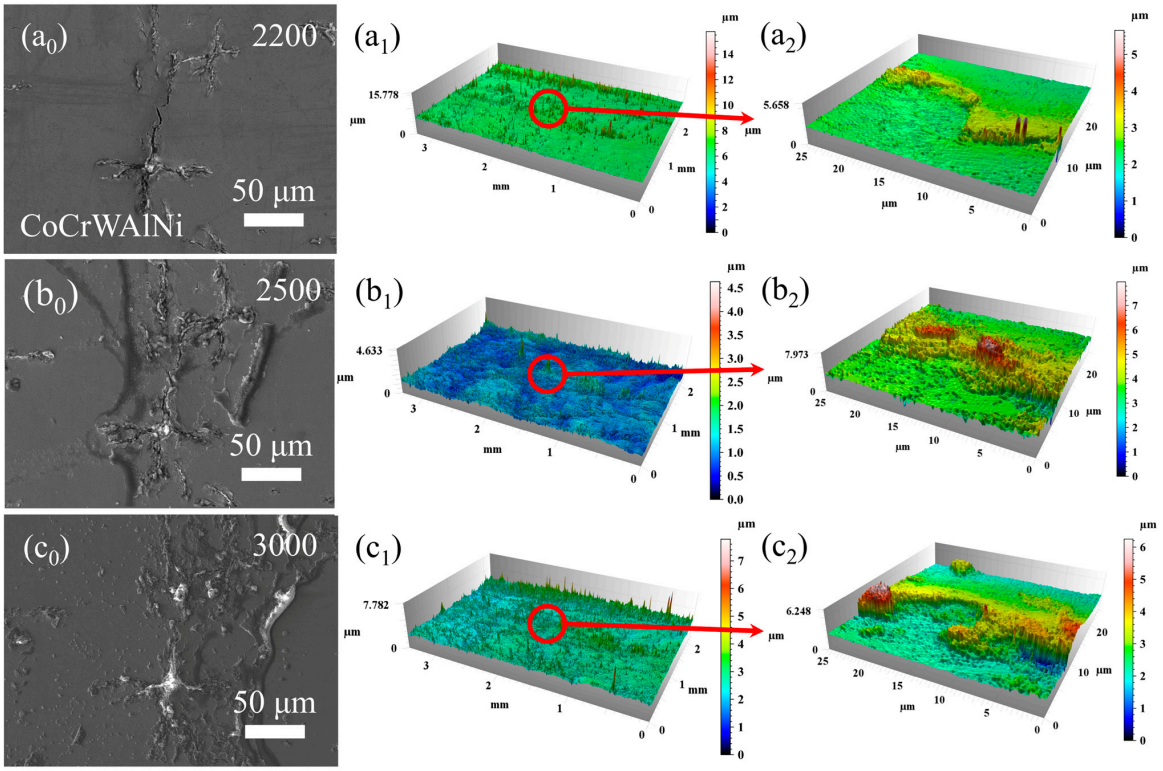


Figure 6. SEM and LSM images of TF racks of CoCrWAlNi at different cycles of (**a$_0$**–**a$_2$**) 2200, (**b$_0$**–**b$_2$**) 2500, (**c$_0$**–**c$_2$**) 3000.

3.3. Oxidation and Cracking During Thermal Fatigue Process

Figure 7 presents high-resolution XPS spectra obtained from the TF surfaces of the CoCrW and CoCrWAlNi alloys. High-resolution scans were acquired for the Cr 2p3/2 and Co 2p3/2 regions. The spectra can be deconvoluted into metallic and oxidized states: Cr (573.1 eV), Cr_2O_3 (577 eV), Co (777.8 eV), and Co_3O_4 (780.3 eV), as shown in Figure 7(a_1,a_2,b_1,b_2). For the CoCrWAlNi alloy, the Al 2p3/2 spectrum was also fitted into two components, corresponding to metallic Al (73 eV) and Al_2O_3 (77.3 eV), while the Ni 3p signal (66.3 eV) was detected as well (Figure 7(b_3)). The high-resolution Ni 2p3/2 spectrum was further deconvoluted into metallic Ni (852.1 eV) and NiO (854.6 eV) (Figure 7(b_4)). Based on the cation fraction analysis of Co, Cr (Figure 8), and their corresponding oxides, the additions of Al and Ni elements promote the formation of a continuous and compact Cr-rich oxide film. This effect is attributed to the enhanced self-diffusivity of Cr [34].

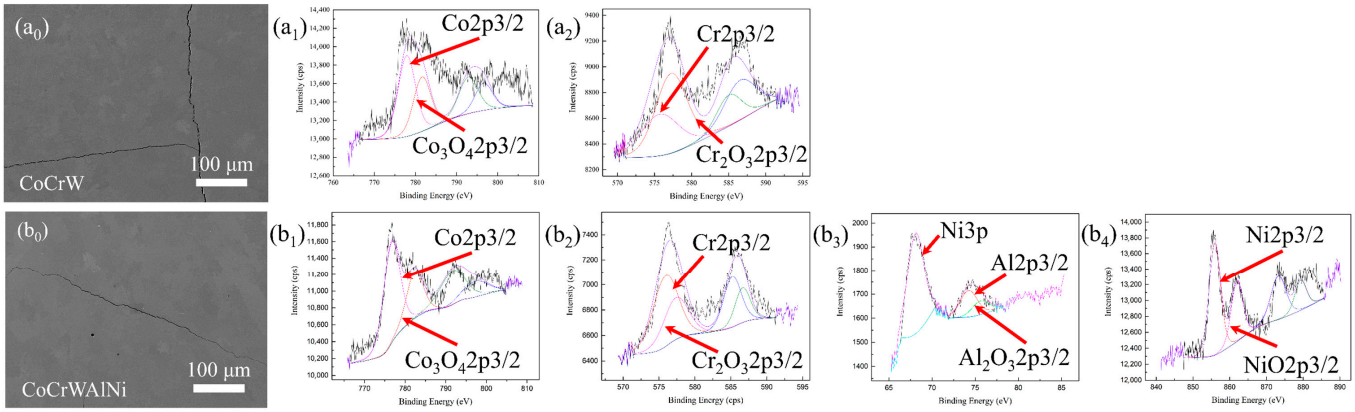


Figure 7. High resolution XPS spectra of the TF surface of (**a_0**–**a_2**) CoCrW, (**b_0**–**b_4**) CoCrWAlNi.

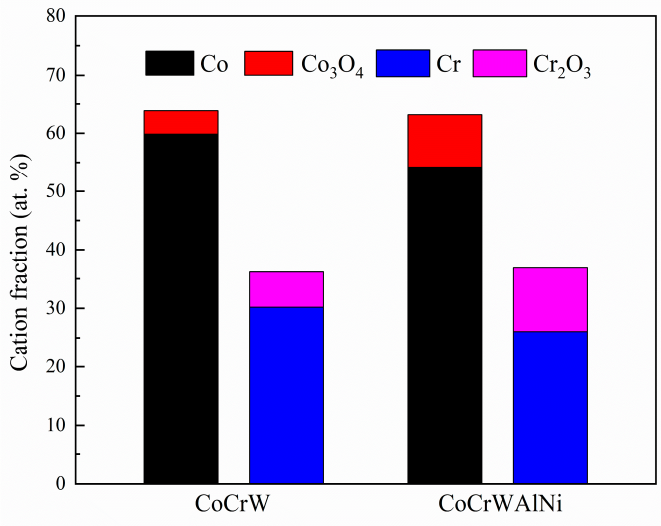


Figure 8. Cation fractions of Co and Cr and their oxides on the surface of the CoCrW and CoCrWAlNi alloys as measured by XPS.

Figures 9 and 10 illustrate the cross-sectional morphologies of the TF damaged surfaces, which reflect the differences in oxidation behavior between the two alloys. The blue line in Figure 9 denotes the scanning path of the line scan. At 1500 TF cycles, a thin and continuous oxide layer was formed on the CoCrWAlNi alloy. In contrast, a significant oxygen signal was detected in the network-shaped eutectic structures of the CoCrW alloy, indicating more severe internal oxidation compared to the CoCrWAlNi alloy. After 3000 TF cycles, cracks had propagated into the interior of both alloys. Notably, such internal oxidation is not

typical of single-phase alloys but is prevalent in multi-phase alloys. This internal oxidation induces substantial internal stress, which adversely impairs the TF resistance of the alloys. Furthermore, oxidation progresses with crack propagation and, in turn, accelerates the crack growth process.

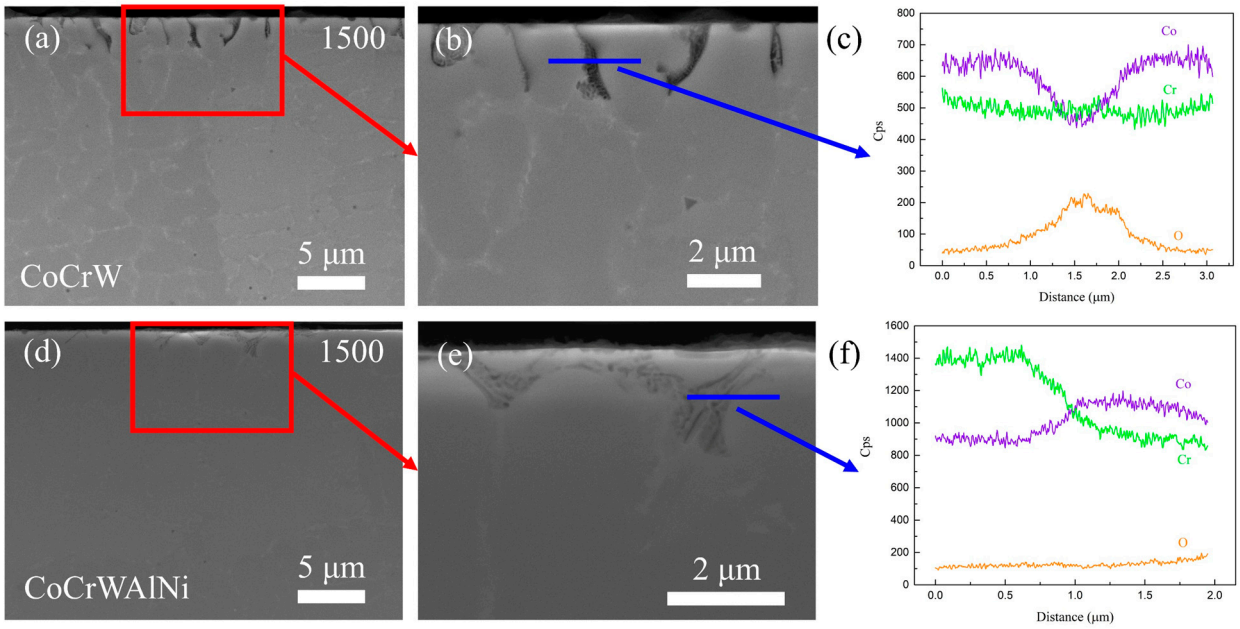


Figure 9. Cross-sectional SEM images and EDS line scanning of the TF surface after 1500 cycles (**a**–**c**) CoCrW; (**d**–**f**) CoCrWAlNi.

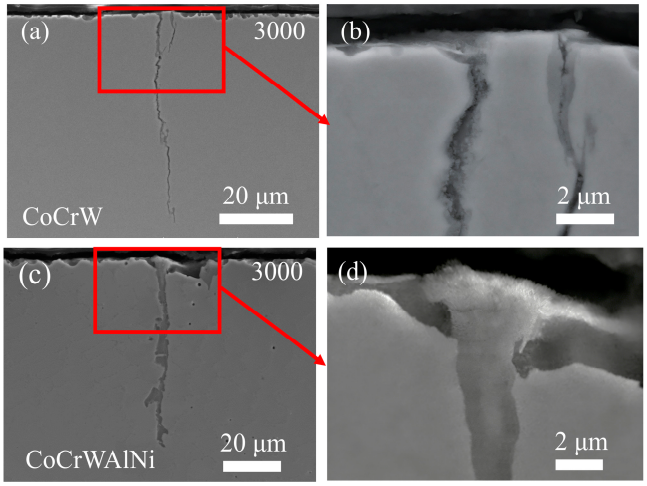


Figure 10. Cross-sectional SEM images of the TF surface after 3000 cycles (**a**,**b**) CoCrW; (**c**,**d**) CoCrWAlNi.

As shown in Figure 11, EBSD and EDS analyses were performed on the specimens after 3000 TF cycles. The CoCrWAlNi alloy exhibited superior TF crack propagation resistance compared to the CoCrW alloy. Inverse pole figure (IPF) maps (Figure 11a,e) represent crystallographic orientations via distinct colors, indicating that both cobalt-based alloys consist of equiaxed dendrites without significant texture. Kernel average misorientation (KAM) maps and geometrically necessary dislocation (GND) calculations reveal the destructive effects of TF cracks on the alloy substrates. Specifically, regions adjacent to cracks and grain boundaries displayed considerably higher KAM values than the matrix, accompanied by enhanced stress concentration (Figure 11b,c,f,g). GND densities were derived from the average KAM values, which are strongly correlated with material

deformation. Notably, the CoCrW alloy exhibited higher KAM and GND values than the CoCrWAlNi alloy, suggesting that more severe TF cracking induces greater deformation and internal strain. As TF cracks propagate rapidly after initiation, oxidation is further accelerated. EDS mappings (Figure 11d,h) confirm the enrichment of oxygen within the TF cracks.

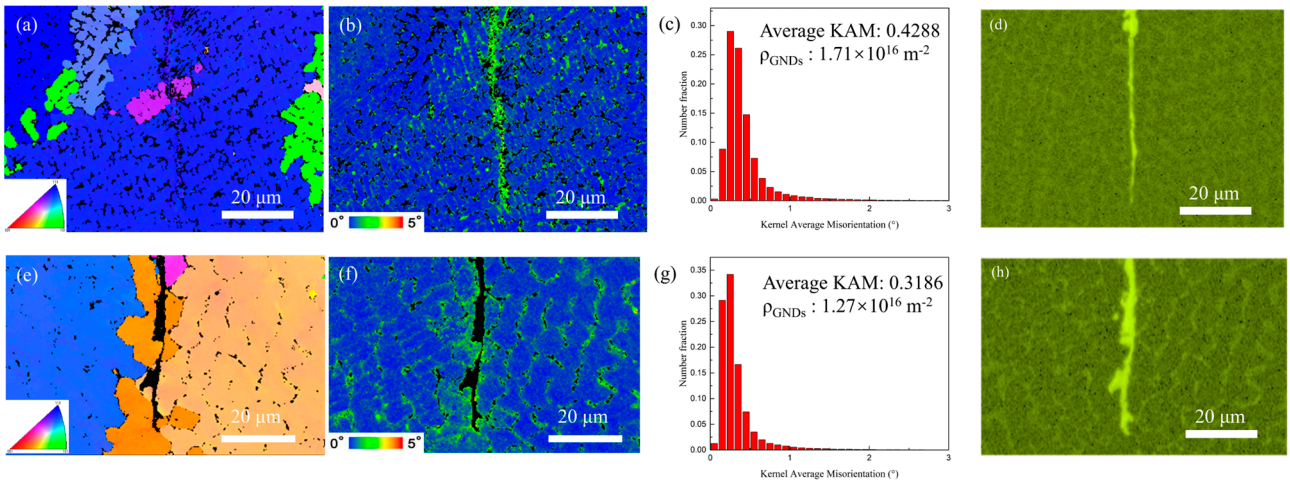


Figure 11. EBSD results of the cross-sectional TF surface (3000 cycles) for IPF Z, KAM, KAM value histograms, and oxygen distribution maps for (**a**–**d**) CoCrW and (**e**–**h**) CoCrWAlNi.

4. Discussion

The TF process involves cyclic thermal shock induced by heating-cooling cycles, which gives rise to thermal stress, plastic strain, oxidation, and elemental diffusion. As detailed in the previous section, the initiation and propagation behaviors of TF cracks have been systematically characterized. In this section, the factors influencing TF resistance will be discussed through stress analysis, with a particular focus on the effects of internal oxidation.

Both alloys consist of a γ-Co matrix and carbide precipitates, where the network-shaped carbides are more susceptible to oxidation than the matrix. This preferential oxidation of carbides leads to internal oxidation and oxygen diffusion along the carbide networks. As illustrated in Figure 8, a thin and continuous external oxide layer forms on the surface of the CoCrWAlNi alloy, while internal oxidation occurs in both alloys—with the CoCrW alloy exhibiting more severe internal oxidation. This phenomenon can be attributed to the additions of Al and Ni elements, which promote Cr diffusion in the matrix. Such enhanced Cr diffusion facilitates the formation of a continuous, thin Cr-rich oxide layer on the surface, rather than the exclusive oxidation of carbides observed in the CoCrW alloy. Nevertheless, the Cr content in the matrix of the CoCrWAlNi alloy is insufficient to form a relatively thick protective oxide film.

Only internal oxidation was considered in the oxidation models of the two alloys. According to Huntz [35], the stress induced by internal oxidation mainly arises from the volume expansion of the oxides (σ_v).

$$\sigma_v = \frac{E_m\left(1-\sqrt[3]{\lambda_{PB}}\right)}{(1-\nu_m)d_m/d_o}, \quad (1)$$

where the subscripts m and o denote the matrix and oxide, respectively. E is the elasticity modulus, ν is Poisson's ratio, d is the grain size, λ_{PB} is the Pilling Bedworth Ratio (Cr_2O_3/Cr 2.07). The related data is listed in Table 3.

Table 3. Physical parameters for internal oxidation.

Alloy	*E*/(GPa)	ν	d_m/μm	d_o/μm
CoCrW	208	0.31	5	0.35
CoCrWAlNi	194	0.38	6	0.25
Co	305 [36]	0.303 [36]	/	/

The oxide volume expansion-induced stresses in the CoCrW and CoCrWAlNi alloys were determined to be 8.41 GPa and 5.01 GPa, respectively. The volume expansion of oxides gave rise to compressive stress within the alloy matrix, which further generated high tensile stress at the Cr_2O_3/Cr/matrix interface. Notably, the calculated stress values exceeded the yield strength of the alloys, which was inconsistent with the corresponding experimental observations. In fact, the stress generated by internal oxidation was partially relaxed via creep deformation, and the deformation rate of polycrystalline materials can be described by the model proposed by Karch [37]. The internal oxidation-induced stress in the CoCrW alloy was significantly higher than that in the CoCrWAlNi alloy, which constituted the dominant factor responsible for the TF failure of the material.

As shown in Figure 10, the strain and stress concentration at the crack tip facilitated oxygen diffusion and oxide formation. Meanwhile, the formed oxides further elevated the local stress, thereby accelerating crack propagation. Cracks tended to nucleate at phase boundaries, while their subsequent growth exhibited a mixed intergranular and transgranular mode, with propagation directions perpendicular to the sample surface. This behavior suggests that the applied stress was sufficiently high to drive cracks to propagate directly through the matrix rather than along preferential pathways. The resistance of the matrix to cracking dominates the overall crack growth behavior. The additions of Al and Ni elements enhanced the stability of the γ-Co matrix, endowing it with superior deformability. Consequently, the matrix was capable of accommodating a higher density of dislocations and sustaining greater crack-tip stress. Therefore, the crack propagation rate of the CoCrWAlNi alloy was lower than that of the CoCrW alloy.

The TF process of the CoCrWAlNi alloy can be divided into four stages. (1) A thin oxide layer forms on the alloy surface. (2) Carbide precipitates are oxidized as oxygen diffuses through the thin oxide layer, leading to the generation of high internal stress within the alloy. (3) Cracks initiate at the oxide–substrate interface under cyclic thermal stress. (4) Oxidation proceeds along the crack paths, which further grow and aggravate stress concentration at the crack tip, thereby promoting crack propagation. By contrast, the TF process of the CoCrW alloy skips the first stage, resulting in the rapid oxidation of carbides.

In summary, the additions of Al and Ni elements to the CoCrW alloy improve ductility and stabilize the γ-Co matrix. The TF resistance is closely associated with the oxidation behavior of the alloy. The CoCrWAlNi alloy possesses a lower carbide fraction than the CoCrW alloy, and a continuous thin oxide layer forms on its surface. These factors are beneficial in suppressing internal oxidation and encouraging crack propagation along phase boundaries.

5. Conclusions

In this study, Al and Ni elements were incorporated into the CoCrW alloy fabricated by DLD to tailor its microstructure and performance. The microstructure, mechanical properties, and TF resistance of the two alloys were systematically characterized, and the evolution behavior and underlying mechanism of the TF process were analyzed in detail. The main conclusions are summarized as follows.

(1) The CoCrWAlNi alloy was composed of γ-Co, $M_{23}C_6$, and M_7C_3 phases, while the ε-Co phase was only present in the CoCrW alloy. The additions of Al and Ni elements reduced the carbide fraction and increased the SFEs, thereby stabilizing the γ-Co matrix. Consequently, the CoCrWAlNi alloy achieved a higher elongation (6%) than the CoCrW alloy (1.75%).
(2) The CoCrWAlNi alloy exhibited superior TF resistance. The alloying elements Al and Ni facilitated the formation of a protective external oxide layer and suppressed internal oxidation, which effectively retarded the initiation of TF cracks.
(3) Oxidation during the TF process was detrimental, and internal oxidation was significantly more harmful than external oxidation with respect to crack initiation. Reducing the carbide content decreased the rapid diffusion path of oxygen and inhibited crack propagation.

Author Contributions: Conceptualization, X.Y. and Z.J.; methodology, X.Y. and Z.J.; software, X.Y. and X.Z.; validation, X.Z. and Y.X.; formal analysis, J.X.; investigation, J.X. and Y.X.; resources, Y.X.; data curation, X.Y. and J.X.; writing—original draft preparation, X.Y.; writing—review and editing, X.Y. and J.X.; visualization, J.X. and Y.X.; supervision, X.Y. and Y.X.; project administration, X.Y. and Y.X.; funding acquisition, X.Y. and Y.X. All authors have read and agreed to the published version of the manuscript.

Funding: This work was supported by the Shanghai "Science and Technology Innovation Action" Promising Star Cultivation-Yangfan Special Project (No. 23YF1428100), Shanghai Industrial Collaborative Innovation (Science and Technology) Project (No. XTCX-KJ-2023-31), Achievement Transformation and Application Project of the "Insight Action" (No. F79C5326).

Data Availability Statement: The original contributions presented in this study are included in the article. Further inquiries can be directed to the corresponding author.

Conflicts of Interest: Authors Xudong Yang, Zixian Jiao, Jiayue Xu and Yi Xie were employed by the company Shanghai Institute of Space Propulsion. The remaining authors declare that the research was conducted in the absence of any commercial or financial relationships that could be construed as a potential conflict of interest.

Abbreviations

The following abbreviations are used in this manuscript:

TF	Thermal fatigue
Ni	Nickel
Cr	Chromium
Al	Aluminum
DLD	Direct laser deposition
SEM	Scanning electron microscope
EDS	Energy dispersive spectroscope
EBSD	Electron backscatter diffraction
XRD	X-ray diffraction
XPS	X-ray photoelectron spectroscopy
LSM	Laser scanning microscope
BSE	Backscattered electron
SFEs	Stacking fault energies
IPF	Inverse pole figure
KAM	Kernel average misorientation
GNDs	Geometrically necessary dislocations

References

1. Gândara, T.; Costa, V.; Dias, J. A novel heat transfer modeling methodology for regenerative cooling in liquid propellant rocket engines. *Case Stud. Therm. Eng.* **2025**, *73*, 106623. [CrossRef]
2. Meng, Q.; Zhang, K.; He, R.; Qu, Z. A review of thermal shock behavior of ceramics: Fundamental theory, experimental methods, and outlooks. *Int. J. Appl. Ceram. Technol.* **2024**, *21*, 3789–3811. [CrossRef]
3. Meiirbekov, M.; Sadykov, M.; Kuandyk, A.; Nurguzhin, M.; Janikeyev, M.; Gulmaira, P.; Mustafa, L.; Yesbolov, N. Multimatrix Composite Materials for Rocket Nozzle Manufacturing: A Comparative Review. *Polymers* **2025**, *17*, 2946. [CrossRef]
4. Li, W.; Cao, R.; Zhu, F.; Yan, Y.; Ma, J.; Zhu, Y. Damage induced bending strength variation and crack initiation mechanism during thermal cycling shock of laser deposited Stellite alloy coating for engine valve. *J. Mater. Res. Technol.* **2025**, *36*, 6062–6074. [CrossRef]
5. Gao, P.-H.; Li, Q.-B.; Chen, B.-Y.; Zhang, B.; Naumov, A.; Wang, Z.-T.; Yang, Z.; Guo, Y.-C. Influence of plasma arc currents on the microstructure and properties of Stellite-20 alloy coatings through plasma transfer arc cladding. *J. Mater. Res. Technol.* **2025**, *36*, 6142–6154. [CrossRef]
6. Tiwari, V.; Mandal, V.; Sarkar, M.; Kumar, A.; Bhagyaraj, J.; Singh, M.K.; Mukherjee, S.; Mondal, K.; Ramkumar, J.; Jain, J.; et al. Enhanced mechanical properties and microstructure of TiC reinforced Stellite 6 metal matrix composites (MMCs) via laser cladding additive manufacturing. *J. Alloys Compd.* **2025**, *1010*, 178001. [CrossRef]
7. Zhao, Y.; Yang, C.; Wang, L.; Wu, Y.; Liu, Y.; Xie, Z.; Fang, Q.; Feng, W.; Liu, H.; Chen, H. Enhancing strength, ductility, and thermal fatigue resistance in Stellite 21 coatings via Mn alloying and Transformation-Induced Plasticity. *Mater. Sci. Eng. A* **2024**, *918*, 147448. [CrossRef]
8. Wu, Y.; Liu, Y.; Chen, H.; Chen, Y.; Li, H.; Cao, X. Developing the ductility and thermal fatigue cracking property of laser-deposited Stellite 6 coatings by adding titanium and nickel. *Mater. Des.* **2019**, *162*, 271–284. [CrossRef]
9. Wu, Y.; Zou, G.; Liu, Y.; A, Z.; Zhao, W.; Wang, W.; Xue, J.; Zhang, Y.; Jia, Q.; Chen, H. Temperature dependence of the tensile and thermal fatigue cracking properties of laser-deposited cobalt-based coatings for brake disc application. *Mater. Sci. Eng. A* **2022**, *858*, 144135. [CrossRef]
10. Li, J.; Zhang, X.; Bu, H.; Qi, H.; Zuo, P.; Li, S.; Li, M. Effects of deep cryogenic treatment on the microstructure evolution, mechanical and thermal fatigue properties of H13 hot work die steel. *J. Mater. Res. Technol.* **2023**, *27*, 8100–8118. [CrossRef]
11. Ou, W.; Xiong, J.; Peng, Y.; Xu, J.; Chen, Z.; Zhang, H.; Li, X.; Yang, J.; Zhang, L.; Mao, G.; et al. Transformation of carbides and mechanisms for cracking in Co-based alloy surfacing layer during thermal fatigue. *Mater. Charact.* **2023**, *201*, 112971. [CrossRef]
12. Wen, J.; Che, H.; Cao, R.; Dong, H.; Ye, Y.; Zhang, H.; Brechtl, J.; Gao, Y.; Liaw, P.K. Evolution of the mechanical properties of a cobalt-based alloy under thermal shocks. *Mater. Des.* **2020**, *188*, 108425. [CrossRef]
13. Guo, H.Y.; Li, Y.M.; Wang, X.G.; Tan, Z.H.; Tan, H.B.; Li, J.G.; Zhou, Y.Z.; Sun, X.F. Influence factors of thermal fatigue behavior of a low-cost third generation Ni-based single crystal superalloy. *Mater. Charact.* **2025**, *224*, 114976. [CrossRef]
14. Li, C.-D.; Yang, H.-Y.; Dong, B.-X.; Chen, D.-L.; Shu, S.-L.; Qiu, F.; Jiang, Q.-C.; Zhang, L.-C. Thermal fatigue failure mechanisms and enhancement strategies of die steel. *J. Mater. Res. Technol.* **2025**, *38*, 4567–4599. [CrossRef]
15. Liu, H.; Qin, Z.; Huang, D.; Wei, C.; Tang, H.; Li, W.; Lei, S. Study of thermal shock properties of $MoSi_2$ modified coatings on Nb-based alloy. *Int. J. Refract. Met. Hard Mater.* **2025**, *133*, 107304. [CrossRef]
16. Wen, J.; Cao, R.; Gao, Y. Mysterious failure in load-free superalloys under repeated thermal shocks. *Acta Mater.* **2020**, *194*, 276–282. [CrossRef]
17. Wen, J.; Cao, R.; Che, H.; Dong, H.; Zhang, H.; Yan, Y.; Gao, Y.; Liaw, P.K. The oxidation effect on the cracking behavior of a Co-based alloy under thermal shocks. *Corros. Sci.* **2020**, *173*, 108828. [CrossRef]
18. Man, Y.; Hua, C.; Huang, T.; Yin, G.; Ma, T.; Zhuang, Y.; He, X.; Xiong, X.; Song, P. Positive effect of large porosity in super-thick thermal barrier coatings on thermal shock resistance and failure mechanisms. *J. Alloys Compd.* **2025**, *1017*, 178792. [CrossRef]
19. Salem, M.; Le Roux, S.; Dour, G.; Vande Put, A. Role of oxidation in thermal fatigue damage mechanisms and life of X38CrMoV5 (AISI H11) hot work tool steel. *Int. J. Fatigue* **2025**, *190*, 108584. [CrossRef]
20. Wagner, C. Theoretical Analysis of the Diffusion Processes Determining the Oxidation Rate of Alloys. *J. Electrochem. Soc.* **1952**, *99*, 369–380. [CrossRef]
21. Gesmundo, F.; Viani, F.; Niu, Y.; Douglass, D.L. Further aspects of the oxidation of binary two-phase alloys. *Oxid. Met.* **1993**, *39*, 197–209. [CrossRef]
22. Viani, F.; Gesmundo, F. The relationships between the different rate constants and the diffusion properties of the oxides in the parabolic oxidation of a metal or a lower oxide to multilayer scales: Application to the oxidation of iron. *Corros. Sci.* **1980**, *20*, 541–554. [CrossRef]
23. Gesmundo, F.; Viani, F.; Niu, Y.; Douglass, D.L. The transition from the formation of mixed scales to the selective oxidation of the most-reactive component in the corrosion of single and two-phase binary alloys. *Oxid. Met.* **1993**, *40*, 373–393. [CrossRef]
24. Gesmundo, F.; Viani, F.; Niu, Y.; Douglass, D.L. An improved treatment of the conditions for the exclusive oxidation of the most-reactive component in the corrosion of two-phase alloys. *Oxid. Met.* **1994**, *42*, 465–483. [CrossRef]

25. Chattopadhyay, B.; Wood, G.C. The transient oxidation of alloys. *Oxid. Met.* **1970**, *2*, 373–399. [CrossRef]
26. Gesmundo, F.; Niu, Y.; Viani, F. Possible scaling modes in high-temperature oxidation of two-phase binary alloys. II: Low oxidant pressures. *Oxid. Met.* **1995**, *43*, 379–394. [CrossRef]
27. Gesmundo, F.; Viani, F.; Niu, Y. The internal oxidation of two-phase binary alloys under low oxidant pressures. *Oxid. Met.* **1996**, *45*, 51–76. [CrossRef]
28. Gesmundo, F.; Viani, F.; Niu, Y. The kinetics of growth and the critical conditions for the formation of the most-stable oxide in the oxidation of binary alloys. *Oxid. Met.* **1994**, *42*, 285–301. [CrossRef]
29. Espevik, S.; Rapp, R.A.; Daniel, P.L.; Hirth, J.P. Oxidation of ternary Co-Cr-W alloys. *Oxid. Met.* **1983**, *20*, 37–65. [CrossRef]
30. Irving, G.N.; Stringer, J.; Whittle, D.P. Effect of the possible fcc stabilizers Mn, Fe, and Ni on the high-temperature oxidation of Co-Cr alloys. *Oxid. Met.* **1974**, *8*, 393–407. [CrossRef]
31. Wallwork, G.R.; Hed, A.Z. Selection of an alloy composition in the ternary Co-Cr-Al system for oxidation resistance. *Oxid. Met.* **1971**, *3*, 243–250. [CrossRef]
32. *ISO-6892-1*; Metallic Materials—Tensile Testing—Part 1: Method of Test at Room Temperature. International Organization for Standardization (ISO): Geneva, Switzerland, 2019.
33. Yang, X.; Li, C.; Zhang, M.; Ye, Z.; Zhang, X.; Zheng, M.; Gu, J.; Zhu, H.; Wang, F. Study on tensile and thermal fatigue behaviors of additively manufactured cobalt-based alloys alloying with Al and Ni. *Mater. Sci. Eng. A* **2022**, *840*, 142914. [CrossRef]
34. Pint, B.A. High Temperature Corrosion of Alumina-forming Iron, Nickel and Cobalt-base Alloys. In *Shreir's Corrosion*; Elsevier: Oxford, UK, 2010; pp. 606–645.
35. Huntz, A.M. Stresses in NiO, Cr_2O_3 and Al_2O_3 oxide scales. *Mater. Sci. Eng. A* **1995**, *201*, 211–228. [CrossRef]
36. Liu, P.; Chen, D.; Wang, Q.; Xu, P.; Long, M.; Duan, H. Crystal structure and mechanical properties of nickel–cobalt alloys with different compositions: A first-principles study. *J. Phys. Chem. Solids* **2020**, *137*, 109194. [CrossRef]
37. Karch, J.; Birringer, R.; Gleiter, H. Ceramics ductile at low temperature. *Nature* **1987**, *330*, 556–558. [CrossRef]

Disclaimer/Publisher's Note: The statements, opinions and data contained in all publications are solely those of the individual author(s) and contributor(s) and not of MDPI and/or the editor(s). MDPI and/or the editor(s) disclaim responsibility for any injury to people or property resulting from any ideas, methods, instructions or products referred to in the content.